JOURNAL OF AIRCRAFT
Vol. 32, No. 6, November–December 1995

Surface Reflective Visualization System Study to Vortical Flow over Delta Wings

S. R. Donohoe,* E. M. Houtman,† and W. J. Bannink‡
Delft University of Technology, Delft, The Netherlands

Evaluation of the surface reflective visualization (SRV) system is conducted using both experimental and numerical simulation techniques. Experimental measurements are made with a spherical five-hole probe utilizing a local look-up calibration algorithm. These data are used to determine the location of the primary vortex core as well as the spanwise integrated density gradient. The numerical simulation technique employs a fast ray tracing algorithm and schlieren system simulation to determine the integrated density gradient distribution over the surface of the wing. The initial numerical flow solution used in the simulation is generated via a computational code based on a finite volume discretization of the three-dimensional conservation law form of the Euler equations. Both the experimental and numerical validation procedures support initial interpretations of SRV images of the compressible vortical flowfield above the lee side of the delta wing. The experimental results of the probe explorations supported the geometric interpretation of the images. The numerical simulation demonstrated that the SRV technique can, indeed, be expected to visualize the embedded crossflow shock existing at transonic flow conditions.

Nomenclature

c_r = root chord, 120 mm
f = focal length
I = illumination
n = refractive index
y_{le} = local spanwise distance from root chord to leading edge
Z_h = length of integration path
κ = Gladstone–Dale constant

Introduction

TO achieve an attractive balance between supersonic cruise performance and maneuverability at high subsonic speeds, modern aircraft designers often utilize highly swept slender wings or delta wings. These aircraft achieve high maneuverability by exploiting the nonlinear lift component generated by the powerful rotating flow existing above the lee surface of the wing when operating at angle of attack. Figure 1 illustrates the characteristic vortical flowfield found above a noncambered sharp leading-edge delta wing operating at moderately high angle of attack. The location of the flow separation lines, reattachment lines, and the core of the vortices, is known to be a complex function of the freestream Mach number, leading-edge sweep angle, leading-edge shape, surface camber, and the Reynolds number. A tertiary vortex embedded under the secondary vortex may also exist under certain conditions. Strong theoretical and numerical support for the presence of a crossflow shock wave embedded under the primary vortex for certain configurations in the high subsonic flow regime has been found (see inset of Fig. 1), but experimental confirmation of this phenomenon has yet to be achieved.[1]

Although complex vortical flows are currently incorporated into the design of high-performance aircraft, they remain an intriguing topic of fundamental aerodynamic research. At a given freestream Mach number the nonlinear lift component generated by existing lee-side vortices will increase with increasing angle of attack up to the point where the vortex breaks down. Vortex breakdown, likely first visualized in a water tunnel in 1954 by Werlé,[2] is commonly described as a transition from an organized vortical flow structure to a large-scale fluctuating turbulent flow. Although some progress has been made in defining the origin of vortex breakdown (i.e., the presence of an adverse pressure gradient and/or surpassing a critical swirl intensity), the physical mechanisms of vortex breakdown remain an issue of debate.

In the incompressible flow regime the breakdown position above the wing is found to move gradually forward with increasing angle of attack. In the compressible regime, however, breakdown has been found to jump suddenly from beyond

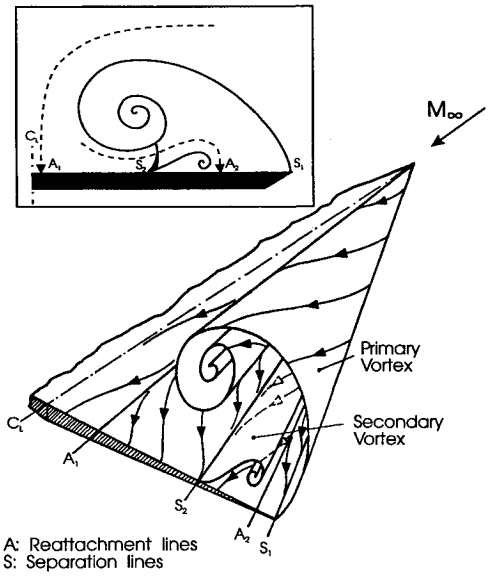

Fig. 1 Characteristic vortical flow above lee surface of a sharp leading-edge delta wing at angle of attack.

Presented as Paper 94-2480 at the AIAA 18th Aerospace Ground Testing Conference, Colorado Springs, CO, June 20–23, 1994; received Feb. 4, 1995; revision received June 21, 1995; accepted for publication June 21, 1995. Copyright © 1995 by the American Institute of Aeronautics and Astronautics, Inc. All rights reserved.

*Research Assistant, Department of Aerospace Engineering, P.O. Box 5058, NL-2600 GB. Student Member AIAA.
†Assistant Professor, Department of Aerospace Engineering, P.O. Box 5058, NL-2600 GB.
‡Associate Professor, Department of Aerospace Engineering, P.O. Box 5058, NL-2600 GB.

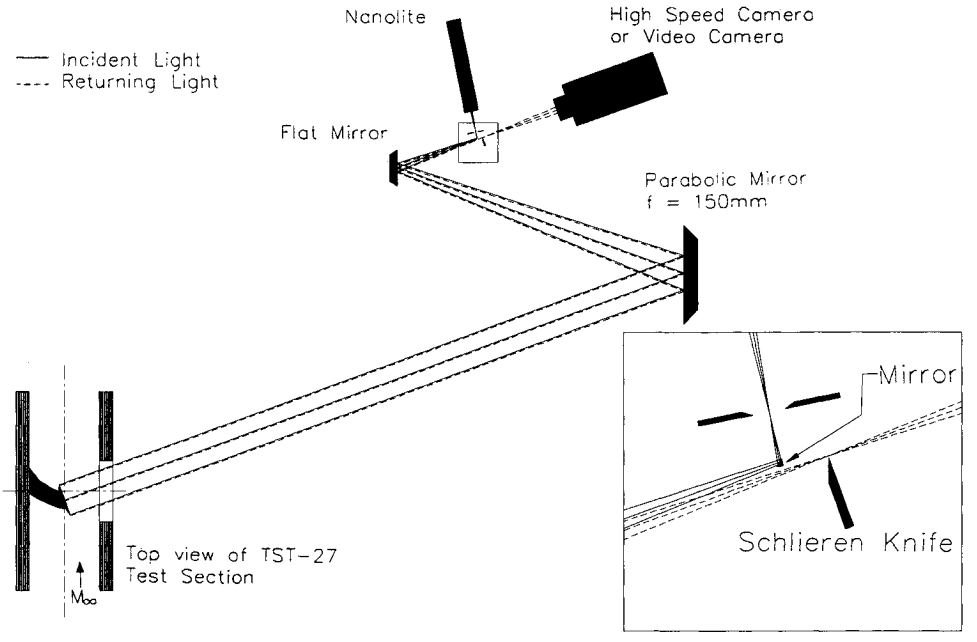

Fig. 2 SRV system configuration.

the trailing edge to as far forward as 50% of the wing chord at a critical angle of attack.[3] The sudden presence of vortex breakdown above the wing, which is often nonsymmetric with respect to the symmetry plane of the wing, can result in severe control problems for the aircraft. The vortex breakdown process is particularly complex in the high subsonic flow regime where the vortex flow is influenced by compressible flow effects such as shock wave/vortex and shock wave/boundary-layer interactions. In his recent survey of the last 40 years of vortex breakdown research, Délery admits that despite its importance for high-speed flight, "the question of shock/vortex interaction and shock-induced breakdown" remains "a largely unexplored field."[4]

To better study this problem the surface reflective visualization (SRV) technique has been developed.[5] This system provides a unique plan-view perspective on the density distribution above a noncambered delta wing. This perspective provides a new opportunity to observe vortices, shock waves, and vortex/shock-wave interactions. Large-scale fluctuations of the often unsteady shock system associated with vortex breakdown can also be visualized by incorporating a high-speed camera into the SRV system configuration. This article will evaluate the SRV technique using both experimental and numerical approaches to establish its viability as a useful new measurement technique.

SRV System

The SRV system is a derivative of a double-pass schlieren/shadowgraph system in which the model surface is itself a component of the optical system (see Fig. 2). The fundamental function of a schlieren system is to provide an image of the density gradient existing perpendicular to a parallel light bundle integrated over the path of that bundle of light. The change in illumination at a location (x, y) in a schlieren image relative to that of the undisturbed image is described by the relation

$$\frac{\Delta I}{I}(x, y) \propto \int_0^L \frac{\partial}{\partial y} n(x, y, z)\, dz \tag{1}$$

where n is linearly coupled to the density via the relation

$$n = 1 + \kappa\rho \tag{2}$$

the schlieren knife edge is in the $x - y$ plane parallel to the x axis, the schlieren knife edge is perpendicular to the y axis,

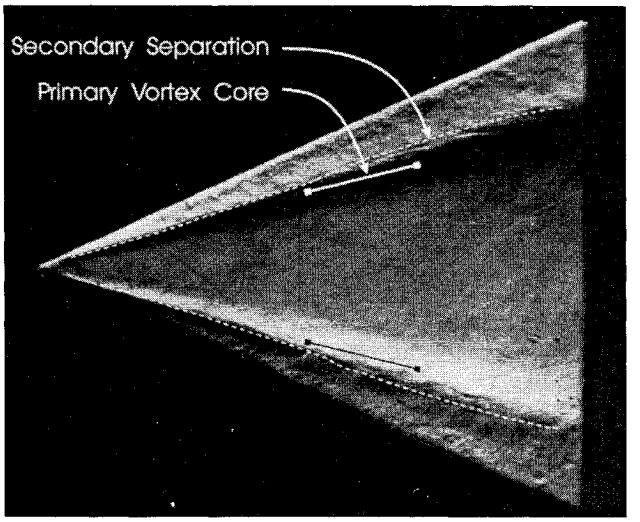

Fig. 3 Experimental SRV image, α = 15 deg, M_∞ = 0.6.

and the z axis is parallel with the path of the light bundle. The constant κ is a characteristic of the gas through which the light passes.[6] In the SRV system configuration used in this study the knife edge is aligned with the x axis parallel to the root chord of the model and the path of the light approaches the model surface perpendicularly along the z axis (see Fig. 5). Thus, the image produced illustrates the distribution of the spanwise density gradient integrated along a path perpendicular to the model surface.

In Figs. 3 and 4 a positive $\partial\rho/\partial y$ is indicated by a lightening of the image and negative $\partial\rho/\partial y$ is indicated by a darkening of the image. Thus, the decreasing integrated density moving outboard through the primary vortex causes the white coloration found between 40 and approximately 65% of the distance to the leading edge on the port side of the wing. The secondary vortex separation lines, determined previously using an oil flow technique, are indicated in these images by dotted lines. In Fig. 4 a sharp line is located outboard of the secondary separation line. This line is an indication of an embedded crossflow shock wave existing between the primary vortex and the wing surface. Also, in Fig. 4, the dark lines intersecting the chord at approximately 80 and 90% of the

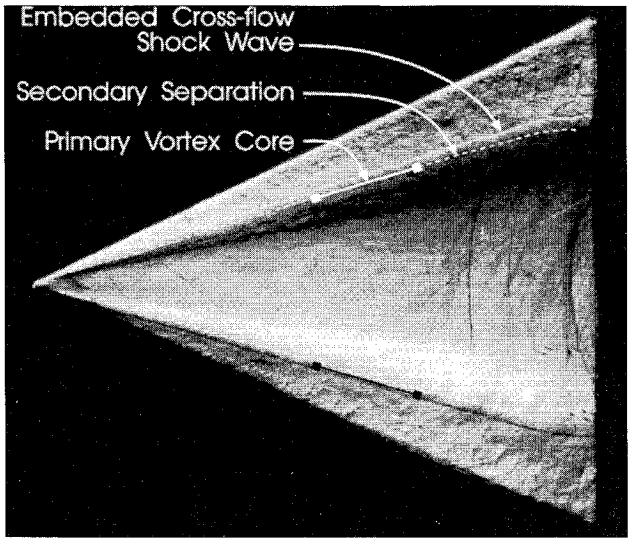

Fig. 4 Experimental SRV image, $\alpha = 15$ deg, $M_\infty = 0.8$.

root chord represent the trailing-edge shock system that has been previously visualized with a side-view transmission schlieren system.[5]

These initial results with the SRV system were encouraging, providing a unique view of spanwise shock distributions above the wing and vortex/shock-wave interactions. Uncertainty remained, however, regarding the proper geometric interpretation of the images created. The double-pass nature of the visualization system caused concern about the influence of light refraction on the geometric accuracy of the final images. While the SRV system seemed to provide a unique new view of embedded crossflow shocks, this conclusion remained tenuous. A validation study was required for the SRV system before further research could be done into the vortex breakdown phenomenon using this technique.

Experimental Analysis

Wind Tunnel and Models

All experiments were performed in the TST-27 transonic–supersonic wind tunnel of the Delft University of Technology High Speed Aerodynamics Laboratory. The TST-27 is a blowdown type of wind tunnel with a maximum stagnation pressure of 4.0×10^5 Pa, a Mach number range from 0.5 up to 4.0, and a tunnel cross section of approximately 280×260 mm. Windows of 295 mm diameter are located in the side walls of the tunnel to allow visual access of the test section.

The model used is noncambered with a chord length of 120 mm, a leading-edge sweep angle of 65 deg, and a sharp leading edge. The model is supported by an adjustable sting in the test section that allows the five-hole probe surveys to be visualized by a side-view transmission schlieren system during the tests. The general structure of the vortex system can, thus, be monitored during the measurements to determine whether the probe is significantly influencing the flowfield (i.e., initiating vortex breakdown). The SRV model is supported, however, on the side wall of the tunnel with a solid support to allow requisite visual access to the upper surface of the model via the side window of the tunnel while the tunnel is running. Because of this model support discrepancy several control tests were done with the five-hole probe above the model with the side mount configuration to ensure flow consistency between the two support configurations used.

Five-Hole Probe Surveys

Test Program

It is not possible to measure a flowfield experiencing vortex breakdown with a five-hole probe due to intrusion influences and/or calibration difficulties. Thus, configurations of Mach number and angle of attack are selected for the validation tests that do not exhibit vortex breakdown above the wing. Tests are made with freestream Mach numbers of 0.6 and 0.8 (with Reynolds numbers of 3.5×10^6 and 4.1×10^6, respectively) at 15-deg angle of attack. Measurements are conducted in two different spanwise planes perpendicular to the wing upper surface on the starboard side of the wing. These planes, extending from approximately 40–100% of the distance to leading edge, are located at $x/c_r = 0.5$ and 0.7 and have a grid spacing of 0.5 and 0.7 mm, respectively (see Fig. 5). An additional measurement plane, extending from the wing centerline to the leading edge with a grid spacing of 1.4 mm, is examined at $M_\infty = 0.8$ and $x/c_r = 0.7$ to control the influence of the grid spacing on the simulation results as well as to provide a more complete picture of the flow characteristics in the spanwise plane.

Experimental Technique

The five-hole probe used for this study is a spherical head probe of 1.6 mm external diameter with pressure taps of 0.2 mm diameter. A previously developed local look-up algorithm yields, for flow angles up to 60 deg, an accuracy of $\pm 3\%$, and ± 0.4 deg in local Mach number and flow angle, respectively.[7] The probe has been recently fitted with miniature fast response piezoelectric pressure transducers that enable the pressure transducers to be housed within the support arm of the probe inside the wind tunnel. This significant reduction in distance between the probe orifices and pressure transducers (approximately 20 cm in the current study and 2.5 m previously) significantly reduces the measurement time

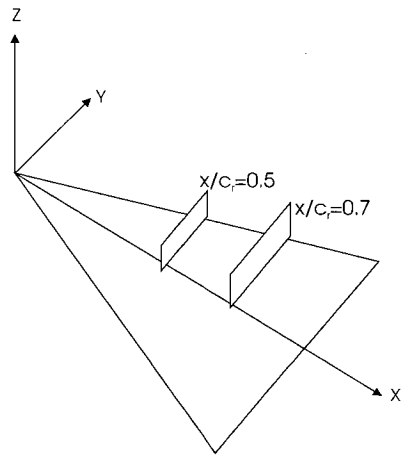

Fig. 5 Illustration of body-fixed Cartesian coordinate system and five-hole probe measurement planes.

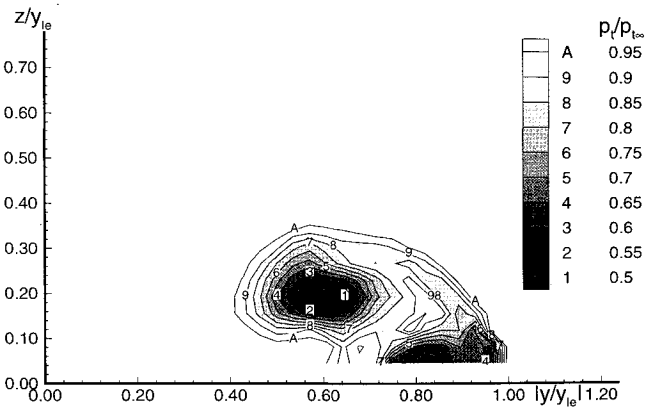

Fig. 6 Experimental spanwise distribution of total pressure, $\alpha = 15$ deg, $M_\infty = 0.8$, $x/c_r = 0.7$.

required per point and allows use of a more refined measurement grid than was previously feasible.

Results

Vortex Core Location

The location of the vortex core in each measurement plane is defined as the location of minimum total pressure. A characteristic contour plot of the total pressure distribution is seen in Fig. 6. The minimum total pressure is located at $y/y_{le} = 0.66$ in both measurement planes when $M_\infty = 0.6$. When $M_\infty = 0.8$, however, the minimum total pressure is located at $y/y_{le} = 0.63$ and $y/y_{le} = 0.61$ in the $x/c_r = 0.5$ and $x/c_r = 0.7$ measurement planes, respectively. This inboard movement with increasing x station is as anticipated due to the trailing-edge effect encouraging the vortex to realign itself with the freestream direction. The control tests made with the model supported on the side wall of the tunnel in the SRV configuration found that the spanwise location of the vortex core remained the same within $y/y_{le} = \pm 0.01$ and the vertical height within $z/y_{le} = \pm 0.02$. These small geometric discrepancies (between 0.4–0.8 mm) can be explained by the inability to correct for dynamic displacement of the side-wall supported model and the probe itself in this configuration due to lack of visual access.

Comparing the probe measurement locations of the primary vortex core with the SRV images in Figs. 3 and 4 reveals that for the case of $M_\infty = 0.6$ the projected vortex core is located within the light colored region of expansion towards the leading edge on the port side of the wing. In contrast, with the higher freestream Mach number of $M_\infty = 0.8$, the edge of the integrated expansion coincides with the spanwise location of the measured vortex core.

Density Distribution

To compare the density distribution measured by the five-hole probe with that visualized by the SRV system the integrated density gradient in the spanwise direction is calculated. Having determined the local Mach number and total pressure, the local density to freestream density ratio is determined by assuming a constant total enthalpy via the relation

$$\frac{\rho}{\rho_\infty} = \frac{p_t}{p_{t_\infty}} \left\{ \frac{1 + [(\gamma - 1)/2]M_\infty^2}{1 + [(\gamma - 1)/2]M^2} \right\}^{1/(\gamma - 1)} \tag{3}$$

The density distribution measured at $x/c_r = 0.7$ when $M_\infty = 0.8$ and $\alpha = 15$ deg with a grid spacing of 1.4 mm is illustrated in Fig. 7. To obtain the spanwise gradient of the integrated density first the local values of ρ/ρ_∞ are integrated along a path perpendicular to the wing surface. The gradient of the integrated density is then calculated via a finite difference

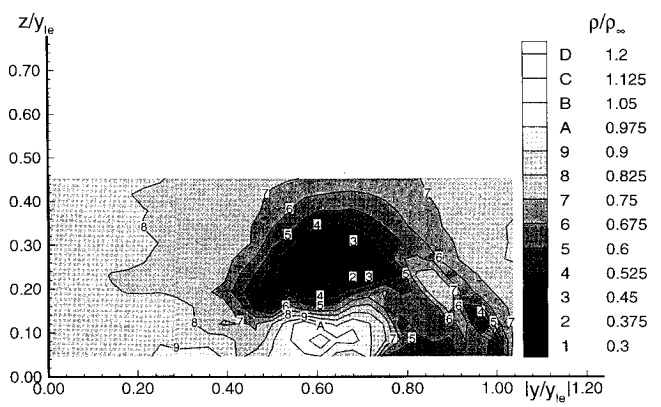

Fig. 7 Experimental spanwise distribution of density, $\alpha = 15$ deg, $M_\infty = 0.8$, $x/c_r = 0.7$.

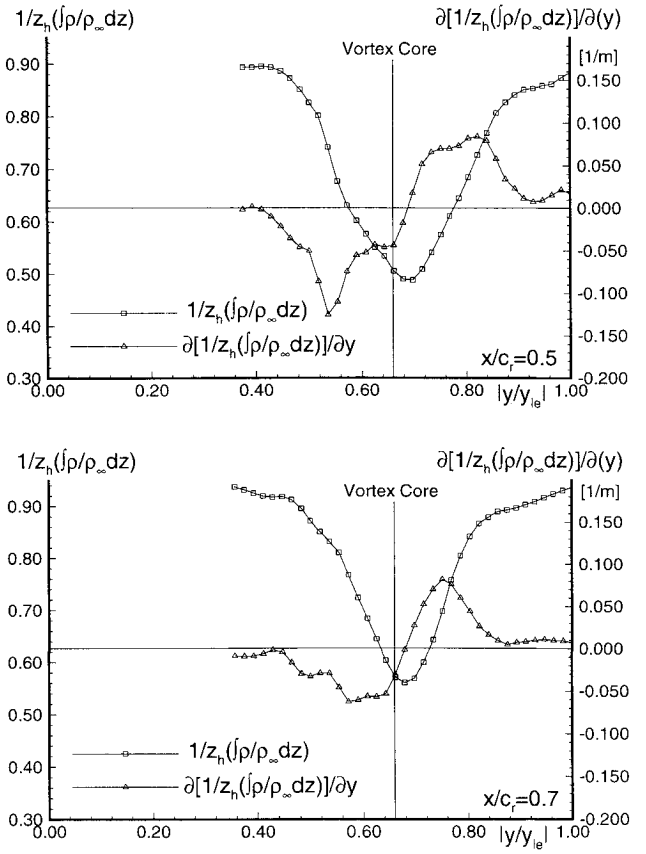

Fig. 8 Experimental spanwise distribution of integrated density and integrated density gradient, $\alpha = 15$ deg, $M_\infty = 0.6$.

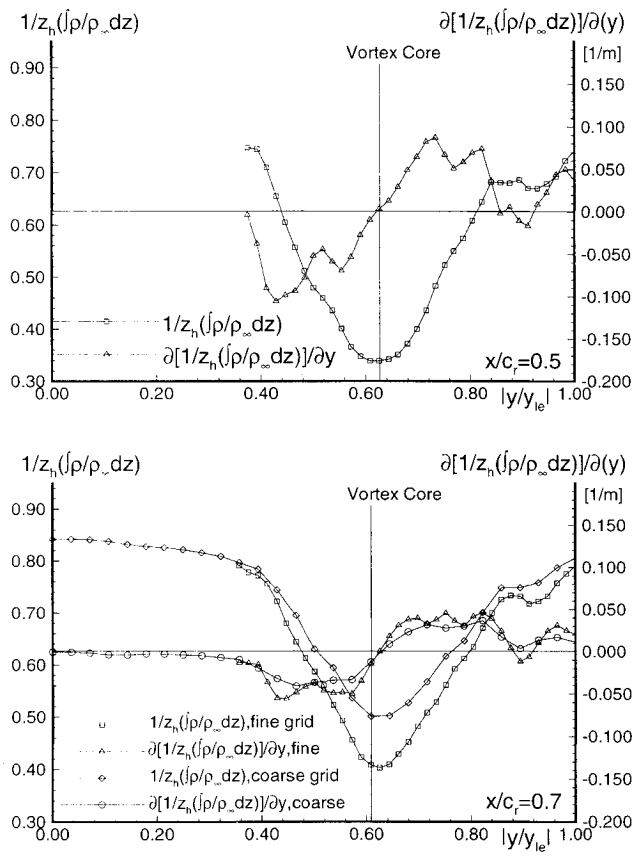

Fig. 9 Experimental spanwise distribution of integrated density and integrated density gradient, $\alpha = 15$ deg, $M_\infty = 0.8$.

discretization. In the calculations several traverses close to the wing surface are neglected due to clear evidence of wing/probe interference (i.e., positive c_p values just above the wing surface).

Figure 8 illustrates the spanwise distribution of both the integrated density and the spanwise gradient of the integrated density at $x/c_r = 0.5$ and $x/c_r = 0.7$ when $M_\infty = 0.6$ and $\alpha = 15$ deg. The integrated density is found to have a minimum at $y/y_{le} = 0.68$ for both chord locations. That this minimum is located slightly outboard of the minimum total pressure mentioned previously can likely be attributed to the presence of the secondary vortex. The transition from white to a darker color on the port side of the wing in Fig. 3 outboard of the location of the primary vortex core is, similarly, likely a result of the influence of the secondary vortex. The negative integrated density gradient inboard of the minimum integrated density and positive gradient outboard is also consistent with the SRV image of Fig. 3.

Figure 9 illustrates the spanwise distribution of both the integrated density and the spanwise gradient of the integrated density at $x/c_r = 0.5$ and $x/c_r = 0.7$ when $M_\infty = 0.8$ and $\alpha = 15$ deg. In the case of $x/c_r = 0.7$ these data are presented for both the fine and coarse measurement grid cases. At this higher freestream Mach number the location of the minimum integrated density is consistent with the location of the minimum total pressure discussed previously. The transition from white to a darker color on the port side of the wing in Fig. 4 is coincident with the spanwise location of the minimum integrated density and the primary vortex core. The influence of the secondary vortex on the image in this case is likely prevented due to the presence of the embedded crossflow shock below the primary vortex. This shock is visualized just outboard of the secondary separation line in Fig. 4. While the secondary vortex separation is likely shock wave induced, the shock appears outboard of the oil flow separation line in the SRV image due to the shock-wave/boundary-layer interaction phenomenon. This phenomenon causes the subsonic boundary layer to separate upstream of the shock wave itself. The schlieren system will also more clearly illustrate the upper part of the crossflow shock wave illustrated in the inset of Fig. 1 because the density gradient perpendicular to the light bundle will be greatest when the light travels parallel with the surface of the shock wave.

Numerical Analysis

Numerical Solution

The computational code is based on a finite volume discretization of the three-dimensional conservation law form of the Euler equations.[8] The code is an extension of a two-dimensional code developed at the Center of Mathematics and Computer Science (CWI) in Amsterdam.[9] The spatial discretization of the Euler equations makes use of the flux difference splitting approach following Roe,[10] whereby physical propagation properties are taken into account to some extent. The calculation of the fluxes at the cell faces is done according to van Leer's monotone upstream-centered schemes for conservation laws (MUSCL) approach with flux limiting, which provides second-order accuracy. The system of discretized equations is solved by a nonlinear multigrid (FAS) technique, with a collective Gauss–Seidel relaxation procedure acting as smoothing method. The computations are performed on a Convex C3820 minisupercomputer.

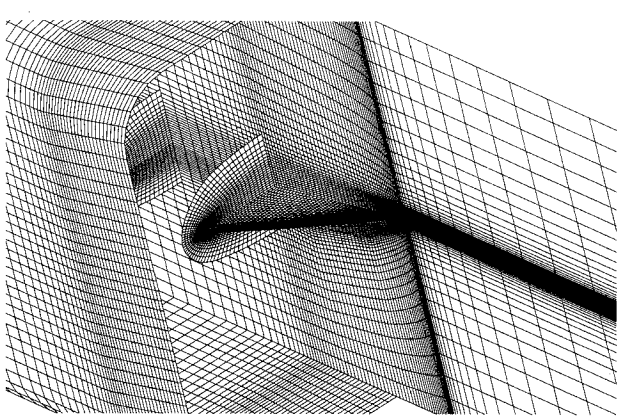

Fig. 10 Computational grid.

To better reproduce the experimental conditions the flow simulations are performed on a computational mesh representing the delta wing in the TST-27 wind tunnel. The grid has a H–O topology, and covers only a half-space due to the symmetry of the flow problem. The number of grid cells is 196,608, which means 96 cells in chordwise direction, 64 cells in spanwise direction, and 32 cells between model surface and wind-tunnel walls. The surface grid along with the grid in the symmetry plane and some cross-planes is shown in Fig. 10. On the surface the grid is conical, preserving good resolution near the apex.

Schlieren Simulation Algorithm

In order to support the interpretation of the experimental schlieren images an algorithm is developed for the construction of schlieren images from computed flowfields. Schlieren images deliver an integrated gradient of the refractive index along the path of the light beam. For a highly three-dimensional flow, gradients in the refractive index caused by certain flow phenomena along the line of sight (LOS), may cancel each other in the integration process. This makes it very difficult to obtain knowledge about the occurrence and the extent of important phenomena such as shocks, vortex cores, etc., in an unknown flowfield, for which no other experimental investigation tools can be used. For a computed flowfield, however, a variety of visualization tools can be used in order to obtain a detailed insight in the flow structure. Construction of schlieren images from these computed flowfields and using the knowledge about the flowfield structure will provide the opportunity to explain refractive-index gradients as a result of certain flow phenomena. Comparison of the simulated schlieren images with experiments under equivalent conditions can be of important assistance in the interpretation of the experimental images.

The schlieren simulation algorithm used here is an extension of a method used for the construction of interferograms, which can be compared on a one-to-one basis with results from a digital holographic interferometry system.[11] The construction of schlieren images consists of the following steps: 1) integration of the refractive-index gradient along the LOS according to Eq. (1) and 2) postprocessing the integrals to produce the desired image. The postprocessing allows such parameters as the desired schlieren knife-edge direction and the sensitivity of the schlieren system to be adjusted.

From Eq. (2) it follows that the refractive index can be replaced by the density ρ, which is one of the quantities available in the computed flowfield. The actual light path is bent due to refractive-index gradients. Formally this path through the flowfield should be traced, and the refractive index gradient (or density gradient) should be integrated along this path, but this is a very expensive procedure computationally. The computational complexity can be reduced considerably by approximating the light path by a straight line perpendicular to the image plane. The similarity between the final numerical simulation images with those of experiment show this to be a reasonable approximation. In order to evaluate integrals along straight lines through a discrete field, an algorithm has been written that calculates the values of the appropriate integrand at certain points, after which the integration is performed according the trapezoidal rule. This process is schematically shown in Fig. 11. The Euler code described

previously uses a grid with hexahedral cells. For the interpolation procedure, each computational cell is subdivided into five tetrahedrals. The integration procedure follows a path along subsequent cell faces of the tetrahedrals. The intersection of the light path with the cell face is determined and the desired quantity is calculated via a linear interpolation between the nodes of the triangular cell face (see Fig. 11). A further simplification of the simulation process is made by changing the order of the differentiation and the integration in Eq. (1). In this way, first an integration of the density for the desired flowfield is performed, which gives a two-dimensional grid at the image plane containing an averaged density. The result is stored and can subsequently be used by image processing software to construct the interferometric phase map or to construct a schlieren image by differentiation of the integrated density field in a direction normal to the schlieren knife edge. The intensity pattern is proportional to the gradient of the integrated density. The latter process is implemented as a module in the visualization package AVS, where the direction of the schlieren knife edge and the intensity level can be adjusted interactively.

Results

Numerical simulations with the Euler code have been performed for freestream Mach numbers of 0.6 and 0.8 and angles of attack of 10 and 15 deg. For these situations the computational method predicts vortices emanating from the sharp leading edges, where the singularity provokes the separation of the inviscid flow. The computed vortical flowfield agrees rather well with experimental observations. The flow quantities in the core region, however, should be considered with caution, because the true viscosity is not modeled correctly by the numerical viscosity of the discretization scheme. Furthermore, it is obvious that the viscous secondary and tertiary separations from the smooth leeward surface and their effects are not modeled. For the cases at $\alpha = 15$ deg a phenomenon similar to vortex breakdown occurs. These solutions are characterized by an unsteady region near the vortex core at the trailing edge, where the flow is directed upstream. The angle of attack at which this phenomenon occurs in the numerical simulations is slightly less than the angle of attack at which vortex breakdown is observed in experiments by oil flow visualization (approximately 18 deg). Calculations at angles of attack above 15 deg failed, due to the rapid upstream movement of the numerical vortex breakdown.

Simulated SRV images with the knife edge parallel to the root-chord are indicated in Fig. 12 for $M_\infty = 0.6$, $\alpha = 10$ deg, in Fig. 13 for $M_\infty = 0.8$, $\alpha = 10$ deg, and in Fig. 14 for $M_\infty = 0.8$, $\alpha = 15$ deg. In these figures the position of the vortex core is also shown, which is obtained by an algorithm that determines the location of minimal total pressure in a large number of cross-planes. It is clear that the vortex core can be observed in a schlieren image at the place where a change from lightening to darkening of the image occurs. The effect of vortex breakdown can be seen in Fig. 14, where the dark and light regions due to the vortices almost disappear

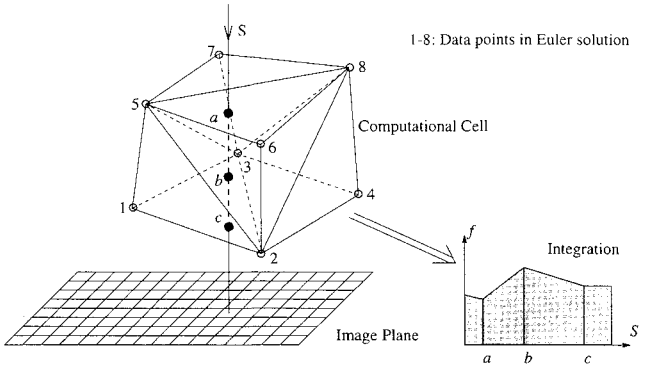

Fig. 11 Schematic view of integration process.

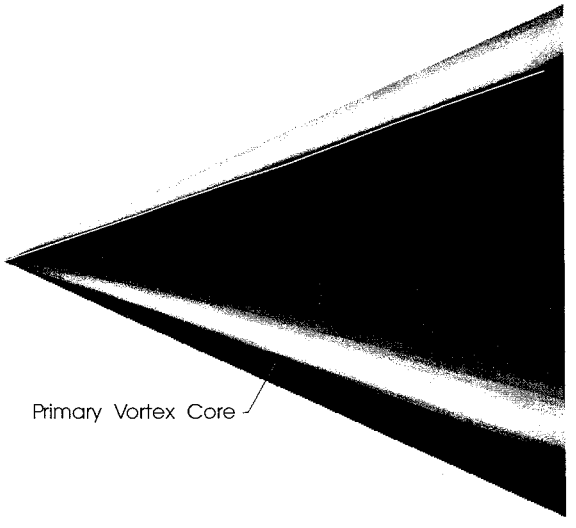

Fig. 12 Numerical simulated SRV image, $M_\infty = 0.6$, $\alpha = 10$ deg.

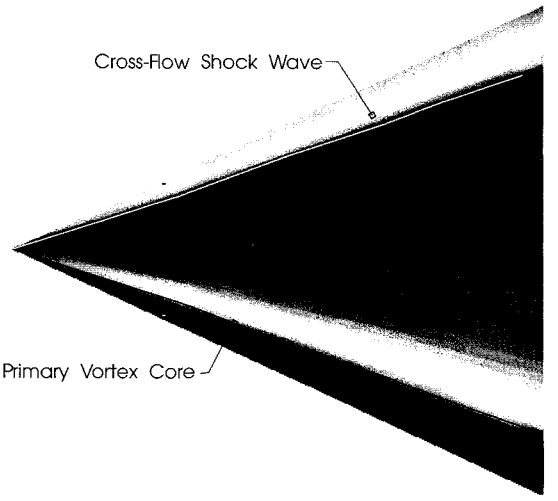

Fig. 13 Numerical simulated SRV image, $M_\infty = 0.8$, $\alpha = 10$ deg.

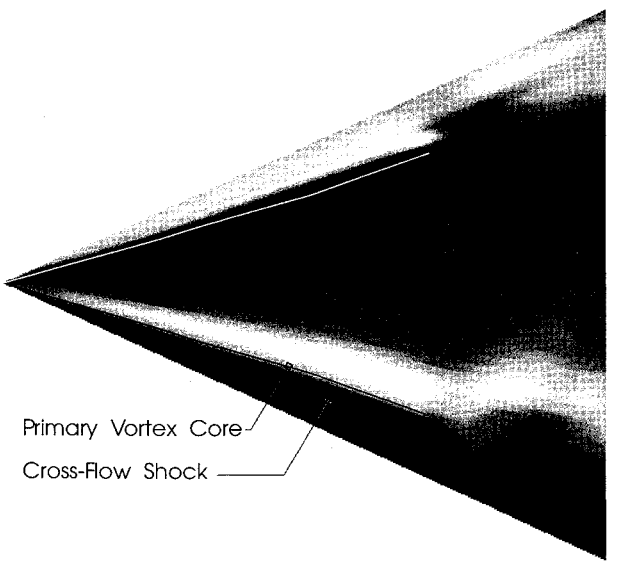

Fig. 14 Numerical simulated SRV image, $M_\infty = 0.8$, $\alpha = 15$ deg.

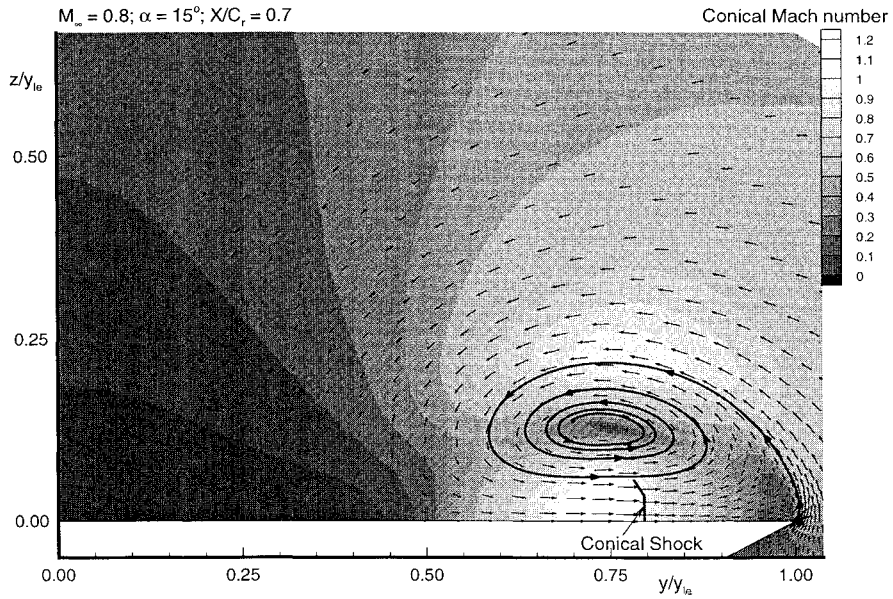

Fig. 15 Numerical distribution of conical Mach number, $M_\infty = 0.8$, $\alpha = 15$ deg, $x/c_r = 0.7$.

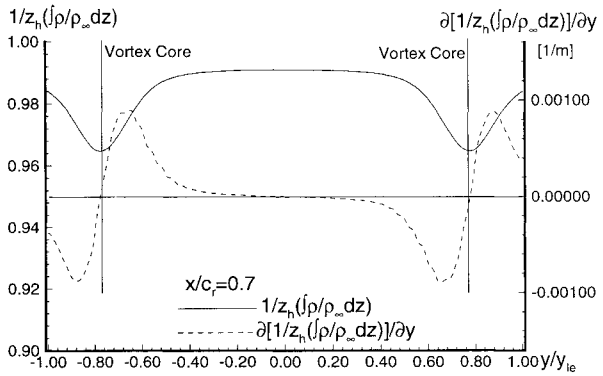

Fig. 16 Numerical spanwise distribution of integrated density and density gradient, $M_\infty = 0.6$, $\alpha = 10$ deg.

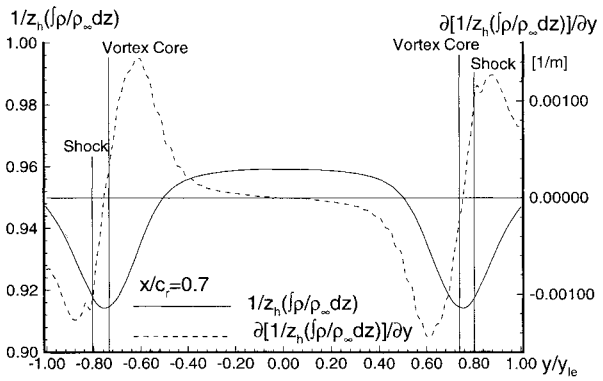

Fig. 17 Numerical spanwise distribution of integrated density and density gradient, $M_\infty = 0.8$, $\alpha = 10$ deg.

downstream of $x/c_r = 0.8$. Because of the vortex breakdown, the circulation of the vortices decreases and subsequently the density gradients. Similar schlieren images were also obtained in experiments with vortex breakdown above the wing.[5]

For $M_\infty = 0.6$ and $\alpha = 10$ deg no embedded shocks occur in the computed flowfield. The spanwise distributions of pressure and conical Mach number at the surface of the model show that for $M_\infty = 0.8$ and $\alpha = 10$ deg a very weak crossflow shock is formed just outboard the position of the vortex core. This shock formation can also be observed in the SRV simulation (Fig. 13), where just outboard of the vortex core a thin black and a white line are visible at the port side and starboard side of the wing, respectively. When $\alpha = 15$ deg the shock is stronger and clearly visible in the simulated SRV image (Fig. 14) upstream of the vortex breakdown ($x/c_r < 0.8$). Downstream of the point of vortex breakdown the shock has disappeared due to the decreased circumferential velocities. Similar lines were also observed in the experimental schlieren images, which makes the interpretation as crossflow shocks more convincing. A plot of the conical Mach number (Mach number based on the velocity component normal to conical ray) together with the direction of the conical (crossflow) velocity is given in Fig. 15. Between the vortex core and the surface a region of supersonic crossflow exists, which is terminated by the indicated conical shock.

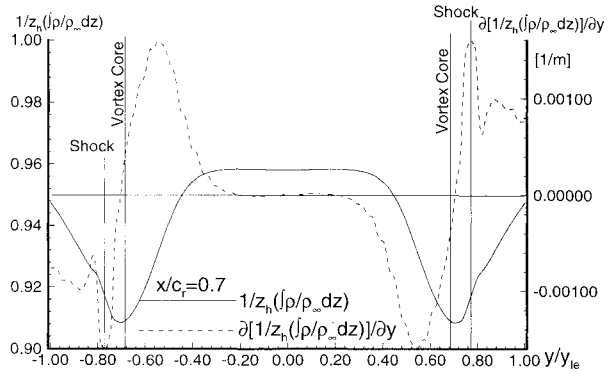

Fig. 18 Numerical spanwise distribution of integrated density and density gradient, $M_\infty = 0.8$, $\alpha = 15$ deg.

In Figs. 16–18 the spanwise distributions of the integrated density and the spanwise density gradient $\partial\rho/\partial y$ are given for $x/c_r = 0.7$. The positions of the vortex cores obtained from the location of the minimal total pressure are also indicated. The location where the density gradient becomes zero roughly coincides with the vortex core position. Furthermore, it can be noted that the density gradients increase with increasing Mach number due to the effect of compressibility. On the other hand, the increase of the density gradient level for increasing angle of attack is not so significant (Figs. 17 and 18). The integrated density for the numerical simulation is higher than the integrated density from the five-hole probe surveys (Figs. 8 and 9). The integration path for the numerical sim-

ulations extends from the upper surface to the wind-tunnel wall, while the integration path for the experiments only covers the measured area. This means that the integrated density for the numerical simulations is higher, because a large part of the integration path lies outside of the vortex region where the density is close to the freestream value. When comparing the spanwise integrated density distributions of the experiment (Fig. 9) with the corresponding distribution of the numerical simulation (Fig. 18), the inboard movement of the primary vortex core due to the secondary vortex can be observed in the shift of the location of the minimal integrated density. The minimum total pressure in the experiment is located at $y/y_{le} = 0.61$, while the location in the numerical simulation is at $y/y_{le} = 0.68$. For $M_\infty = 0.8$ the conical shocks can be observed as the peaks in the distributions of the density gradients.

Conclusions

The viability of the application of the SRV system for visualizing the integrated density gradient existing above a noncambered delta wing in a compressible flowfield is established. Analysis of the system using both experimental and numerical techniques demonstrates the qualitative accuracy of the images produced. Future plans for application of the SRV system include a parametric study of vortex breakdown for various combinations of M_∞ and α to define the geometry of the vortex breakdown mechanisms, vortex/shock-wave interactions, and of the shock waves themselves.

Acknowledgments

The authors would like to thank R. J. P. Boon and M. Oledal for their efforts in developing the fast ray tracing algorithm and in the analysis of the five-hole probe measurements, respectively. The technical support of E. W. de Keizer and F. J. Donker Duyvis is also acknowledged.

References

[1]Elsenaar, A., Hjelmberg, L., Bütefisch, K. A., and Bannink, W. J., "The International Vortex Flow Experiment," *Validation of Computational Fluid Dynamics*, CP-437, AGARD, 1988 (Paper 9).

[2]Werlé, H., "Quelques Résultats Expérimentaux sur les Ailes en Flèches, aux Faibles Vitesses, Obtenus en Tunnel Hydrodynamique," *La Recherche Aéronautique*, Vol. 41, 1954, pp. 15–21.

[3]Muylaert, J. M., "Effect of Compressibility on Vortex Bursting on Slender Delta Wings," von Kármán Inst. for Fluid Dynamics, Project Rept. 1980-21, Rhode St. Genèse, Belgium, 1980.

[4]Délery, J. M., "Aspects of Vortex Breakdown," *Progress in Aerospace Sciences*, Vol. 30, No. 1, 1994, pp. 1–59.

[5]Donohoe, S. R., and Bannink, W. J., "The Utilization of a High Speed Surface Reflective Visualization System in the Study of Transonic Flow over a Delta Wing," *Wall Interference, Support Interference and Flow Field Measurements*, CP-535, AGARD, 1994 (Paper 8).

[6]Merzkirch, W., *Flow Visualization*, Academic, London, 1987.

[7]Houtman, E. M., and Bannink, W. J., "The Calibration and Measuring Procedure of a Five-Hole Hemispherical Head Probe in Compressible Flow," Dept. of Aerospace Engineering, Delft Univ. of Technology, Rept. LR-585, Delft, The Netherlands, 1989.

[8]Houtman, E. M., and Bannink, W. J., "Experimental and Numerical Investigation of the Vortex Flow over a Delta Wing at Transonic Speed," *Vortex Flow Aerodynamics*, CP-494, AGARD, 1991 (Paper 5).

[9]Koren, B., and Spekreijse, S. P., "Multigrid and Defect Correction for the Efficient Solution of the Steady Euler Equations," *Research in Numerical Fluid Mechanics*, edited by P. Wesseling, Vol. 17 of *Notes on Numerical Fluid Mechanics*, Viewig, Brunswick, Germany, 1987, pp. 87–100.

[10]Roe, P. L., "Approximate Riemann Solvers, Parameter Vectors and Difference Schemes," *Journal of Computational Physics*, Vol. 43, 1981, pp. 357–372.

[11]Lanen, T., and Houtman, E. M., "Comparison of Interferometric Measurements with 3-D Euler Computations for Circular Cones in Supersonic Flow," AIAA Paper 92-2691, 1992.